

Characteristics of remnant radio galaxies detected in the deep radio continuum observations from the SKA pathfinders

Sushant Dutta^{1,2,*}, Veeresh Singh¹, C. H. Ishwara Chandra³, Yogesh Wadadekar³ and Abhijit Kayal^{1,2}

¹Physical Research Laboratory, Ahmedabad, 380009, Gujarat, India.

²Indian Institute of Technology Gandhinagar, Palaj, Gandhinagar, 382355, Gujarat, India.

³National Centre for Radio Astrophysics, TIFR, Post Bag 3, Ganeshkhind, Pune 411007, India.

*Corresponding author. E-mail: sushantd@prl.res.in

MS received 27 April 2022; accepted 15 July 2022

Abstract. The cessation of AGN activity in radio galaxies leads to a remnant phase during which jets are no longer sustained, but lobes can be detected for a period of time before they fade away due to radiative and dynamical energy losses. The time-scale of the remnant phase and AGN duty cycle are vital to understanding the evolution of radio galaxies. In this paper, we report new band-3 observations with the upgraded Giant Meterwave Radio Telescope (uGMRT) for five remnant radio galaxies. Our uGMRT observations reveal emission of low-surface-brightness in all five remnants with 400 MHz surface brightness in the range of 36–201 mJy arcmin⁻². With band-3 uGMRT observations, we discover wing-shaped radio morphology in one of our sample sources. Using radio observations at 150 MHz, 325 MHz, 400 MHz, and 1.5 GHz, we model the radio spectral energy distributions (SEDs) of our sample sources with the continuous injection-off model (CI_{OFF}), that assumes an active phase with continuous injection followed by a remnant phase. We obtain total source ages (t_s) in the range of 20.3 Myr to 41.4 Myr with t_{OFF}/t_s distributed in the range of 0.16 to 0.63, which in turn suggests them to belong to different evolutionary phases. We note that, in comparison to the remnants reported in the literature, our sample sources tend to show lower spectral ages that can be explained by the combined effects of more dominant inverse Compton losses for our sources present at the relatively higher redshifts and possible rapid expansion of lobes in their less dense environments.

Keywords. galaxies: active—galaxies: jets—radio continuum: galaxies—galaxies: evolution.

1. Introduction

Radio galaxies, a subclass of active galactic nuclei (AGN), exhibit highly collimated bipolar jets supplying plasma to radio lobes at large distances of hundreds of kilo-parsecs (see [Hardcastle & Croston, 2020](#); [Saikia, 2022](#)). The radio jets launched from the vicinity of an accreting super-massive black hole (SMBH) offer a direct probe to the status of AGN activity. The multi-frequency radio observations have demonstrated that the AGN activity in galaxies is only a phase (‘active phase’) lasting for a few tens of million years ([Dwarakanath & Kale, 2009](#); [Parma et al., 2007](#); [Sari-palli, 2012](#)). After the cessation of AGN activity, the outflowing jets are no longer sustained, which results in the stoppage of plasma supply to radio lobes. Therefore, the cessation of AGN activity in radio galaxies leads to a dying or remnant phase during which radio lobes can still be detected for a relatively short

period of time before they fade away due to energy losses via radiative and dynamical processes ([Murgia et al., 2011](#)). The small samples of remnants ([Mahatma et al., 2018](#); [Jurlin et al., 2021](#)) and the serendipitous discovery of individual remnant radio galaxies (hereafter remnants), e.g., B2 0924+30 ([Cordey, 1987](#); [Shulevski et al., 2017](#)), J021659-044920 ([Tamhane et al., 2015](#)), blob1 ([Brienza et al., 2016](#)) and NGC 1534 ([Duchesne & Johnston-Hollitt, 2019](#)), WISEA J152228.01+274141.3 ([Lal, 2021](#)) etc., mainly detected in the low-frequency observations, led to the notion of remnants being rare sources. Remnants are also detected in the radio sources classified as the double-double radio galaxies (DDRGs) exhibiting two pairs of lobes resulting from the two different episodes of AGN-jet activity. In DDRGs, a new pair of inner lobes driven by the current phase of AGN-jet activity appears before the disappearance of the old pair of outer lobes representing the remnant phase of the previous episode of

AGN-jet activity (Saikia & Jamrozy (2009); Nandi & Saikia (2012); Morganti (2017) and references therein). In our study, we consider remnant sources with no apparent episodic AGN-jet activity. Notably, such remnants seem to be even rarer than the DDRGs (Mahatma *et al.*, 2019; Jurlin *et al.*, 2020). The rarity of remnants has conventionally been attributed to the rapid energy losses at work in relic lobes. Albeit, the timescale over which a remnant can be detected, varies from source to source and depends on various factors such as the source size, magnetic field in the lobes and the large-scale environment (Turner, 2018). The evolution of radio galaxies in their remnant phase is not well understood due to their paucity.

Also, with an aim to constrain the AGN duty cycle and evolutionary models, there have been attempts to perform systematic searches for the remnants (see Godfrey *et al.*, 2017; Brienza *et al.*, 2017; Mahatma *et al.*, 2018). However, such studies often face limitations imposed by the selection criteria and the flux density limits of radio observations. For instance, using Ultra-Steep Spectrum (USS; $\alpha_{74\text{ MHz}}^{1.4\text{ GHz}} < -1.2$, where $S_\nu \propto \nu^\alpha$) selection criterion Godfrey *et al.* (2017) found that only $\leq 2\%$ of their sample sources are remnant candidates. Brienza *et al.* (2017) argued that the use of a single criterion is likely to miss a fraction of remnants, and both morphological as well as spectral criteria ought to be used for the identification of full remnant population. Mahatma *et al.* (2018) emphasized that the absence of a radio core in deep radio observations can be considered as a reliable selection criterion for remnants, irrespective of their radio morphology and spectral behaviour. In their sample of 127 sources with $S_{150\text{ MHz}} \geq 80\text{ mJy}$ and radio size $\geq 40''$, Mahatma *et al.* (2018) found only 11 remnants with no detected radio core in deep (noise-rms $\sim 0.02\text{ mJy beam}^{-1}$) 6 GHz observations. More recently, Jurlin *et al.* (2021) noted that a feeble radio core representing a dying AGN activity can still be present in a remnant and identified only 13 remnants in their sample of 158 sources. Notably, despite the concerted efforts, the studies based on the sensitive low-frequency radio observations in the deep fields, have yielded only small samples with remnant fraction limited to 5%–10% (see Mahatma *et al.*, 2018; Quici *et al.*, 2021; Jurlin *et al.*, 2021).

Further, remnants selected using morphological criteria are of large angular sizes *i.e.*, $\geq 30''$, where a limit on the minimum size is placed for deciphering the morphological details. Hence, morphologically selected remnants are inherently biased towards the remnants of more powerful large-size radio galaxies. Using the spectral curvature criterion, Singh *et al.* (2021) identified remnants of small angular sizes ($< 30''$) and found them to be more abundant, which is consistent with

the theoretical models. For instance, using the ‘Radio AGNs in Semi-Analytic Environments’ (RAiSE) dynamical model, Shabala *et al.* (2020) showed that the models assuming a power law distribution of jet kinetic powers and source ages can explain the observed fraction of remnants and their distributions of flux density, angular size and redshift. In fact, the power law distribution of jet kinetic powers predicts more number of small-size remnants. Thus, the remnant population appears more diverse than that envisaged from the small samples of large-size remnants discovered earlier. Hence, it becomes important to study individual remnant sources and estimate various source parameters such as magnetic field, remnant age, AGN duty cycle and their large-scale environments. The detailed study of individual remnant sources can help us to understand the evolutionary scenario at work in different sources. In this paper, we study five remnant sources using multi-frequency radio observations.

This paper is organized as follows. In Section 2. we provide the details of radio observations. The sample selection criteria and source characteristics are described in Section 3.. In Section 4. we describe the radio SED modelling, spectral age determination of our sample remnants, and their comparison with the remnants reported in the literature. In Section 5. we discuss the potential of deep and wide radio continuum radio surveys planned with the Square Kilometer Array (SKA) and its pathfinders. The results and conclusions of our study are presented in Section 6..

In this paper, we use the cosmological parameters $H_0 = 70\text{ km s}^{-1}\text{ Mpc}^{-1}$, $\Omega_m = 0.3$, and $\Omega_\Lambda = 0.7$. Radio spectral index α is defined by assuming power law spectrum ($S_\nu \propto \nu^\alpha$, where S_ν denotes the flux density at frequency ν).

2. Radio observations

For our study, we used band-3 observations from the upgraded Giant Metrewave Radio Telescope (uGMRT, Gupta *et al.*, 2017), along with the auxiliary radio observations available at 325 MHz from the legacy Giant Metrewave Radio Telescope (GMRT, Swarup, 1991), 144 MHz observations from the LOw Frequency ARray (LOFAR, van Haarlem *et al.*, 2013) and 1.5 GHz observations from the Jansky Very Large Array (JVLA Perley *et al.*, 2011). All our remnant sources are located within a small region of 2.3 deg^2 of the XMM–Large Scale Structure (XMM–LSS) field. In Table 1, we list the basic details of the radio observations. We give a brief description of these observations in the following subsections.

Table 1: Summary of radio observations

| Telescope | band (MHz) | ν_{central} (MHz) | noise-rms (mJy beam ⁻¹) | beam-size ('' × '') |
|-----------|---------------|---------------------------------|--|------------------------|
| LOFAR | 120–168 | 144 | 0.28–0.39 | 7.5×8.5 |
| GMRT | 309–341 | 325 | 0.15 | 10.2×7.9 |
| uGMRT | 250–500 | 400 | 0.03 | 6.7×5.3 |
| JVLA | 994–2018 | 1500 | 0.016 | 4.5×4.5 |

2.1 Band-3 uGMRT radio observations

Our band-3 (250 MHz – 550 MHz) uGMRT observations were performed on 11 September 2017 (proposal code 32_066; PI: C.H. Ishwara-Chandra) in full synthesis mode with nearly 10 hours of total observing time. To obtain the deepest possible image, these observations were limited only to one pointing centered at RA = 02^h 26^m 45^s.0 and DEC = -04° 41' 30''.0 in the *XMM-LSS* field. The observations were acquired in a standard manner by observing the flux calibrators 3C48 and 3C147 for 15–20 minutes at the beginning and end of the observing session, respectively. The phase calibrators 0116-0208 and 0323+055 were observed for nearly 5 minutes with scans inter-leaved with 30 minutes scans of the targeted field. The uGMRT radio data were reduced using a pipeline based on the Common Astronomy Software Applications (CASA¹) routines. We followed the standard data reduction procedure that involved flagging bad data, calibrating visibilities, imaging of calibrated visibilities, and several iterations of self-calibration. The final primary beam corrected image achieves a median noise-rms of 30 $\mu\text{Jy beam}^{-1}$. As expected, the noise-rms is lowest ($\sim 20 \mu\text{Jy beam}^{-1}$) in the central region, while a higher noise-rms ($\sim 40 \mu\text{Jy beam}^{-1}$) is seen around bright sources and in the peripheral regions. The synthesized beam-size is 6''.7 × 5''.3. Using the Python Blob Detector and Source Finder (PyBDSF; Mohan & Rafferty (2015)) algorithm, we detected a total number of 2332 sources at $\geq 5\sigma$ over the full sky-area of 2.3 deg². More details on the data reduction and creation of the source catalogue can be found in a companion paper (Kayal et al. 2022, JoAA, *accepted*).

2.2 Auxiliary radio observations at 144 MHz, 325 MHz and 1.5 GHz

To build radio spectral energy distributions (SEDs) of our remnants, we utilized radio observations available at other frequencies over the widest range. We used 144 MHz LOFAR observations available in the *XMM-LSS* field (Hale et al., 2019). The LOFAR observations

centered at RA = 35° and Dec = -4.5° cover $\sim 27 \text{ deg}^2$ sky-area. The final mosaiced image achieves noise-rms down to 0.28 mJy beam⁻¹ in the central regions while median noise-rms is 0.394 mJy beam⁻¹. The LOFAR observations have a resolution (7''.5 × 8''.5), similar to our band-3 uGMRT observations.

The region of our band-3 uGMRT observations is also covered with the 325 MHz observations performed with the legacy GMRT equipped with software correlator giving 32 MHz instantaneous bandwidth (Proposal: 20_006; PI: Y. Wadadekar). The mosaiced 325 MHz image centred at RA = 02^h 21^m 00^s and DEC = -04° 30' 00'' covers 12.5 deg² sky-area in the *XMM-LSS* field. The 325 MHz mosaiced image has an average noise-rms of 150 $\mu\text{Jy beam}^{-1}$ and synthesized beam-size of 10''.2 × 7''.9. More details about 325 MHz GMRT observations can be found in Singh et al. (2014).

We also utilized 1.5 GHz JVLA observations reported by Heywood et al. (2020). The 1.5 GHz observations performed with the VLA in B-configuration using wide-band (0.994–2.018 GHz) continuum mode cover 5.0 deg² sky-area overlapping with the NIR VIDEO region in the *XMM-LSS* field (Jarvis et al., 2013). The mosaiced image has nearly uniform noise-rms with a median value of $\sim 16 \mu\text{Jy beam}^{-1}$ and synthesized beam-size of 4''.5 × 4''.5. The JVLA observations with the better resolution are efficient in revealing structural details. Although, while building radio SEDs we ensure that the JVLA observations do not suffer with the missing flux issue wherein diffuse emission of low-surface-brightness can be missed due to its higher resolution. We compare JVLA flux densities with those from the 1.4 GHz NVSS, whenever available, and we use NVSS flux densities in case of the missing flux issue. With its large beam-size of 45'' NVSS observations can efficiently detect the diffuse emission of low-surface-brightness emission.

We note that the sky region of our band-3 uGMRT observations is also covered with the 240 MHz, 610 MHz GMRT observations (Tasse et al., 2007) and 74 MHz VLA observations (Tasse et al., 2006). In principle, these observations can be useful in building radio SEDs, however, we found that, unexpectedly, 240 MHz and 610 MHz flux densities are systematically underestimated (see Singh et al., 2021). Hence, we prefer not to use 240 MHz and 610 MHz GMRT observations. Also, 74 MHz VLA observations yielding noise-rms of 32 mJy beam⁻¹ are too shallow to detect our relatively faint sources. Therefore, in our study, we used radio observations mainly from the LOFAR at 144 MHz, the GMRT at 325 MHz, the uGMRT at 400 MHz, and the JVLA at 1.5 GHz.

¹<https://casa.nrao.edu/>

Table 2: Remnant sample

| Source Name | $S_{150\text{ MHz}}^{\text{int}}$ (mJy) | $S_{325\text{ MHz}}^{\text{int}}$ (mJy) | $S_{400\text{ MHz}}^{\text{int}}$ (mJy) | $S_{1.4\text{ GHz}}^{\text{int}}$ (mJy) | $\alpha_{150\text{ MHz}}^{325\text{ MHz}}$ | $\alpha_{400\text{ MHz}}^{1.5\text{ GHz}}$ | $SB_{400\text{ MHz}}$ (mJy arcmin ⁻²) | z | Size (kpc('')) | $\log L_{400\text{ MHz}}$ |
|-------------------|---|---|---|---|--|--|---|-----------|----------------|---------------------------|
| GMRT022318-044526 | 33.9±1.0 | 20.2±2.2 | 12.1±1.4 | 1.70±0.10 | -0.67±0.15 | -1.48±0.10 | 106 | 1.15±0.17 | 643 (78) | 25.99 |
| GMRT022338-045418 | 7.04±0.3 | 3.7±0.7 | 3.1±0.7 | 0.6±0.09 | -0.83±0.25 | -1.24±0.21 | 36 | 0.81±0.01 | 200 (26.5) | 25.29 |
| GMRT022723-051242 | 45.7±0.8 | 21.1±1.1 | 15.8±0.5 | 2.20±0.30 | -0.98±0.07 | -1.49±0.11 | 201 | 0.87±0.07 | 255 (33) | 26.06 |
| GMRT022737-052139 | 6.3±0.8 | 3.7±0.60 | 3.3±0.3 | 0.6±0.07 | -0.69±0.27 | -1.29±0.11 | 56 | 0.62±0.13 | 190 (28) | 25.25 |
| GMRT022802-041417 | 37.3±0.9 | 19.5±1.0 | 16.2±0.5 | 2.4±0.2 | -0.84±0.07 | -1.44±0.07 | 127 | 0.44±0.05 | 216 (38) | 25.19 |

3. The remnant sample and band-3 uGMRT observations

In this subsection, we describe the sample selection criteria and the characteristics of our remnant sources.

3.1 Remnant sample and selection criteria

Our five remnant sources studied in this paper are taken from Singh *et al.* (2021) and Dutta *et al.* 2022 (*under review*). We list the basic parameters, *i.e.*, flux densities, surface brightness, radio sizes, redshifts, and 400 MHz radio luminosities of our sample sources in Table 2. All the five remnant sources are selected by using the spectral curvature criterion, *i.e.*, $\alpha_{150\text{ MHz}}^{325\text{ MHz}} - \alpha_{325\text{ MHz}}^{1.5\text{ GHz}} \geq 0.5$. Using 150 MHz LOFAR, 325 MHz GMRT and 1.4 GHz JVLA observations Singh *et al.* (2021) demonstrated that the remnant sources of small angular sizes (<30'') often lacking morphological details in the radio images of 5'' – 10'' angular resolution, can be identified by using spectral curvature criterion ($\alpha_{\text{low}} - \alpha_{\text{high}} \geq 0.5$). We note that our five remnant sources also satisfy morphological criteria, *i.e.*, diffuse emission of low-surface-brightness (36–201 mJy arcmin⁻² at 400 MHz, see Table 2) and an absence of core in the high frequency 3.0 GHz VLA Sky Survey (VLASS; Lacy *et al.*, 2020) images. The morphological criteria alone can enable us to make robust identification of remnants irrespective of their spectral characteristics (Hota *et al.*, 2011; Mahatma *et al.*, 2018). Therefore, our sources satisfying both morphological and spectral criteria can be regarded as the confirmed remnants.

Further, we note that unlike most of the remnant sources reported in the literature, our sample sources are relatively faint (150 MHz flux density in the range of 6.3 mJy to 37.3 mJy) and reside at relatively higher redshifts ($z \geq 0.44$) (see Table 2). It is worth mentioning that most of the individually studied remnant sources (*e.g.*, Brienza *et al.*, 2016; Shulevski *et al.*, 2017; Duchesne & Johnston-Hollitt, 2019) as well as the remnants derived from the LOFAR observations are relatively bright, *i.e.*, $S_{150\text{ MHz}} > 80$ mJy and extended ($\geq 40''$) (see Mahatma *et al.*, 2018; Jurlin *et al.*, 2021). Therefore, our sample of relatively faint and small-size remnants allow us to probe a different phase space.

3.2 Characteristics of our remnants

In the following subsections, we describe radio morphologies and characteristics of our sample sources. Our new 400 MHz uGMRT observations discover the wing-shaped radio morphology in GMRT022338-045418 (see Figure 1). To compare the radio morphological details at different frequencies, we plot radio contours of 400 MHz uGMRT, 325 MHz GMRT and 1.5 GHz JVLA emissions onto the corresponding optical *i* band images from the Hyper Suprime-Cam Subaru Strategic Program (HSC-SSP²) (see Figure 2, *left panel*).

3.2.1 GMRT022318-044526: This source shows a clear double-lobed radio morphology with a total end-to-end projected size of 78'' that corresponds to the physical size of 643 kpc at the redshift $z = 1.15 \pm 0.17$ of the potential host. The deep 1.5 GHz JVLA observations detect no core but only two lobes that appear edge-brightened similar to the FR-II radio galaxies. Our new 400 MHz uGMRT observations revealed nearly the same structures that were seen in the previous 325 MHz observations (see Figure 2, *top left panel*). Based on the radio contours overlaid on the HSC-SSP *i* band image, a galaxy J022318.1-044520.7 matching close to the centroid of the low-frequency radio emission, is identified as the potential host with an *i* band magnitude (m_i) 24.09 ± 0.08 and photometric redshift (z_{phot}) 1.15 ± 0.17 .

3.2.2 GMRT022338-045418: The band-3 uGMRT image of GMRT022338-045418 shows a wing-shaped radio morphology (see Figure 1), wherein the northern (upper) component resembles a back-flow-like feature, while the southern (lower) component shows a double-peaked emission. This source has very low surface-brightness emission (36 mJy arcmin⁻² at 400 MHz) such that the southern component is completely undetected in the 1.5 GHz JVLA image, while 325 MHz GMRT image of relatively low resolution (10''.2 × 7''.9) shows only north-south elongation with no apparent structures (see Figure 2, *middle left panel*).

²<https://hsc.mtk.nao.ac.jp/ssp/>

Interestingly, the northern component which resembles with a backflow tail in the 400 MHz uGMRT image clearly shows two peaks in the 1.5 GHz JVLA image (see Figure 2, *middle left panel*). Thus, we find that both northern and southern components have two-peak emission, which is commonly seen in the winged radio galaxies classified as the Z-shaped and X-shaped radio sources, wherein diagonally opposite bright peaks correspond to primary lobes, and fainter peaks correspond to secondary lobes, possibly from the previous episode of AGN jet activity (Lal *et al.*, 2019; Bera *et al.*, 2022).

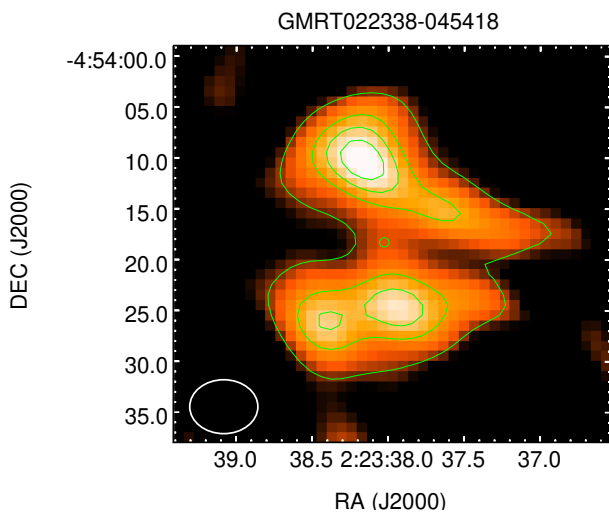


Figure 1: The band-3 uGMRT image of remnant source GMRT022338-045418. For a better representation of intensity distribution, radio contours (in green colour) are overplotted onto the corresponding false colour radio image. The radio contours are shown at $\sigma \times (3, 6, 10, 15, \dots)$ levels. The centroid position is marked with a small green circle. The uGMRT beam-size of $6''.7 \times 5''.3$ is shown in the bottom left corner.

We note that the discovery of wing-shaped radio morphology in GMRT022338-045418 is credited to the sensitivity and resolution of band-3 uGMRT observations that are adequate to detect faint diffuse radio emissions. The total flux density at 400 MHz of this source is only 3.1 ± 0.5 mJy, while northern and southern components have a flux density of 1.62 ± 0.3 mJy and 1.48 ± 0.3 mJy, respectively. The lack of its complete detection in all but band-3 observations poses a challenge in characterizing this source. For instance, a spectral index map requires images at more than one widely separated frequencies with similar angular resolutions. Also, with the present set of radio observations we cannot rule out if wing-shaped radio morphology is the result of two individual double-lobe radio sources located close to each other. Deeper radio observations of higher resolution are needed to examine if this source consists of two individual radio sources.

Although, given the lack of optical counterparts matching with individual lobes and a backflow-like feature seen in the band-3 image (see Figure 2, *left panel*) suggest that the wing-shaped morphology is unlikely to be the result of two individual double-lobed radio sources coincidentally placed adjacent to each other. We note that there is no detected optical counterpart close to the centroid of the band-3 radio morphology (see Figure 2). However, within a radius of $10''$ there are two optical sources, *i.e.*, a relatively bright source J022337.7-045414.8 towards the north-west with $m_i = 22.29 \pm 0.01$ and photometric redshift (z_{phot}) 0.81 ± 0.01 , and a faint source J022338.2-045418.6 towards the east with $m_i = 24.99 \pm 0.05$ and photometric redshift (z_{phot}) 2.75 ± 0.56 . Because radio galaxies generally host in bright ellipticals, we assumed the brighter optical counterpart J022337.7-045414.8 as the potential host.

3.2.3 GMRT022723-051242: The radio morphology of this source resembles a double-lobed source, but the two lobes are not well resolved due to its small angular size of $33''$. We note that a separate point radio source J022723.2-051223.8 is located close to its northern side (see Figure 2, *left panel*). Due to its proximity, the point radio source contaminates the emission of the remnant source at 150 MHz, 325 MHz and 400 MHz as the spatial resolution is somewhat coarser at these frequencies. To accurately determine the flux density of our remnant source, we removed the contamination of the point radio source by considering its 1.5 GHz flux density from the JVLA image and extrapolating it to the lower frequencies by assuming a spectral index of -0.7 . The 1.5 GHz JVLA radio contours of our remnant show two emission peaks each apparently corresponding to the northern and southern lobes, respectively. It is worth noting that the southern peak coincides with a foreground galaxy (J022722.9-051250.6) having $m_i = 19.90 \pm 0.05$ and $z_{\text{phot}} = 0.26 \pm 0.10$. From the current observations, it is unclear if the foreground galaxy also contaminates and to what extent. Although considering the relaxed radio morphology of our remnant with an evident diffusion of emission along the direction perpendicular to the jet-axis, the foreground galaxy is unlikely to give rise to any significant contamination. Also, the ultra-steep radio spectrum towards high-frequencies ($\alpha_{400 \text{ MHz}}^{1.5 \text{ GHz}} = -1.49 \pm 0.11$) suggests only minimal contamination from the foreground galaxy, if it exists. Based on the radio contours, in particular from the 1.5 GHz JVLA overlaid on the *i* band optical image, we consider J022723.1-051242.9 as a potential host with $m_i = 23.02 \pm 0.01$ and $z_{\text{phot}} = 0.87 \pm 0.07$. However, another galaxy J022722.9-051242.8, located close to its centroid, cannot be ruled out from being a plausible host. Our new uGMRT radio observations show ra-

dio morphology similar to that seen with the 325 MHz GMRT and 1.5 GHz JVLA observations.

3.2.4 GMRT022737-052139: The radio morphology of this source shows east-west elongation. The high resolution 1.5 GHz JVLA image indicates the double-lobe-like structure (see Figure 2, *left panel*). The two lobes are not well resolved due to the small angular size (28'') of this source. Our new uGMRT observations show emission consistent with the 325 MHz GMRT observations. With radio contours overlaid on the *i* band optical image we identify J022737-052139 as a potential host with $m_i = 24.17 \pm 0.03$ with $z_{\text{phot}} = 0.62 \pm 0.13$. With a total size of 190 kpc this source is the smallest in our sample. The strong spectral curvature and low surface brightness of 56 mJy arcsec⁻² at 400 MHz suggest it to be a remnant source.

3.2.5 GMRT022802-041417: This source is hosted in a nearby bright ($m_i = 19.45 \pm 0.01$) elliptical galaxy with a photometric redshift of 0.44 ± 0.05 . The angular size (38'') of this source corresponds to the total projected linear size of 216 kpc. Due to its relatively small angular size, 325 MHz and 400 MHz observations do not reveal clear structures. However, 1.5 GHz JVLA image showing east-west elongation and two tentative peaks infer it to be a double-lobed source (see Figure 2, *left panel*).

4. Spectral ages

In this section, we estimate the spectral ages of our remnants and compare them with the remnants already studied in the literature.

4.1 SED modelling

We derive the spectral ages of our remnants via modelling their SEDs with physically motivated models. We note that the radio spectrum of an active radio galaxy can be characterized by the continuous injection model (CI model, Kardashev (1962); Jaffe & Perola (1973)) that assumes continuous replenishment of radio lobes at a constant rate for the duration of t_{ON} . The relativistic particles emitting radio emission have power law energy distribution ($N(E) \propto E^{-p}$) which results in a power law radio spectrum with an index of $\alpha_{\text{inj}} = (p - 1)/2$. Due to the energy-dependent cooling rate of relativistic particles, the radio spectrum develops a break during the active phase itself, such that the spectral index above ν_b steepens to the value of $\alpha_{\text{inj}} - 0.5$, where α_{inj} is typically found in the range of -0.5 to -0.8. As the radio source evolves, the break frequency (ν_b) shifts progressively towards the lower frequencies. The rela-

tion between source age (t_s) and break frequency ν_b can be expressed as below (see Komissarov & Gubanov, 1994; Slee *et al.*, 2001; Parma *et al.*, 2007).

$$t_s = 1590 \left[\frac{B_{\text{eq}}^{0.5}}{(B_{\text{eq}}^2 + B_{\text{CMB}}^2) \sqrt{\nu_b(1+z)}} \right] \text{Myr} \quad (1)$$

where t_s is the total source age, B_{eq} and $B_{\text{CMB}} = 3.25(1+z)^2$ are equipartition magnetic field and inverse Compton equivalent magnetic field, respectively, in the unit of μG , and ν_b is the break frequency in GHz above which spectrum steepens from the initial injection spectral index. We note that the spectral age calculation assumes a uniform magnetic field strength across all the emitting regions, and it also assumes that the magnetic field remains constant during the radiative cooling process. Further, the model considers only radiative losses without accounting for the losses due to expansion.

To estimate the age of remnants, we use continuous injection off (CI_{OFF}) model (Komissarov & Gubanov, 1994) that considers remnant phase after switching off the continuous injection phase lasting for the duration of t_{ON} . In the remnant phase, a new break appears at higher frequencies ($\nu_{b, \text{high}}$) beyond which spectrum drops exponentially. As the remnant phase progresses, $\nu_{b, \text{high}}$ shifts towards the lower frequencies. The ratio of $\nu_{b, \text{low}}$ and $\nu_{b, \text{high}}$ depends on the duration of remnant phase (t_{OFF}) *w.r.t.* the total source age as given by the following formula.

$$\frac{t_{\text{OFF}}}{t_s} = \left(\frac{\nu_{b, \text{low}}}{\nu_{b, \text{high}}} \right)^{0.5} \quad (2)$$

where t_s is the total source age and can be expressed as $t_s = t_{\text{ON}} + t_{\text{OFF}}$. It is obvious that $\nu_{b, \text{low}}$ would be lower than $\nu_{b, \text{high}}$ as $t_{\text{OFF}} < t_s$. However, for a very old remnant, $\nu_{b, \text{high}}$ would appear sufficiently close to $\nu_{b, \text{low}}$. We note that the computation of spectral age requires knowledge of magnetic field strength (see Eqn 1). We estimate magnetic field strength by assuming equipartition of minimum energy between particles and magnetic field and use the following equation.

$$B_{\text{eq}}[\text{G}] = \left(\frac{24\pi}{7} u_{\text{min}} \right)^{1/2} \quad (3)$$

where minimum particle energy (u_{min}) can be calculated using Equation 4 with an approximation of isotropic particle distribution (see Govoni & Feretti, 2004).

$$u_{\text{min}} \left[\frac{\text{erg}}{\text{cm}^3} \right] = \xi(\alpha, \nu_1, \nu_2) (1+k)^{4/7} (\nu_0[\text{MHz}])^{-4\alpha/7} \times (1+z)^{(12-4\alpha)/7} (I_0[\text{mJy arcsec}^{-2}])^{4/7} (d[\text{kpc}])^{-4/7} \quad (4)$$

Table 3: Spectral ageing and source parameters

| Source Name | α_{inj} | d (kpc) | I_0 (mJy arcsec $^{-2}$) | $\xi(\alpha, \nu_1, \nu_2)$ | u_{min} (erg cm $^{-3}$) | B_{eq} (μ G) | $\nu_{b, low}$ (GHz) | $\nu_{b, high}$ (GHz) | t_s (Myr) | t_{ON} (Myr) | t_{OFF} (Myr) | $\frac{t_{OFF}}{t_s}$ | χ^2_{red} |
|-------------------|----------------|-----------|-----------------------------|-----------------------------|-----------------------------|---------------------|----------------------|-----------------------|----------------------|----------------------|----------------------|-----------------------|----------------|
| GMRT022318-044526 | -0.40 | 188 | 0.029 | 3.79×10^{-12} | 6.61×10^{-13} | 2.66 | 0.255 | 3.60 | $20.3^{+2.5}_{-2.8}$ | $15.2^{+1.9}_{-1.7}$ | $5.1^{+1.0}_{-1.2}$ | 0.25 | 1.94 |
| GMRT022338-045418 | -0.54 | 187 | 0.010 | 2.50×10^{-12} | 1.24×10^{-12} | 3.66 | 0.702 | 4.32 | $24.3^{+2.7}_{-3.6}$ | $14.5^{+1.7}_{-1.5}$ | $9.8^{+1.9}_{-1.5}$ | 0.40 | 1.09 |
| GMRT022723-051242 | -0.62 | 197 | 0.056 | 1.72×10^{-12} | 7.35×10^{-13} | 2.80 | 0.251 | 10.9 | $33.2^{+3.8}_{-3.6}$ | $28.0^{+3.3}_{-3.1}$ | $5.2^{+1.5}_{-1.8}$ | 0.16 | 1.08 |
| GMRT022737-052139 | -0.54 | 94 | 0.016 | 2.50×10^{-12} | 4.37×10^{-13} | 2.17 | 0.875 | 3.89 | $27.5^{+4.3}_{-3.6}$ | $14.5^{+4.2}_{-3.1}$ | $13.0^{+1.1}_{-1.6}$ | 0.47 | 1.01 |
| GMRT022802-041417 | -0.56 | 157 | 0.035 | 1.72×10^{-12} | 3.03×10^{-13} | 1.80 | 0.812 | 2.05 | $41.4^{+2.8}_{-2.2}$ | $15.4^{+2.3}_{-1.9}$ | $26.0^{+1.1}_{-1.0}$ | 0.63 | 1.08 |

where parameter ξ depends on the spectral index ($\alpha < 0$ is considered for the observed spectrum) and spectrum is integrated over frequencies ν_1 and ν_2 that correspond to 10 MHz and 100 GHz, respectively, which in turn correspond to a minimum Lorentz factor (γ_{min}) 10 and maximum Lorentz factor (γ_{max}) 10^5 . We use ξ values from the Table 1 of Govoni & Feretti (2004). The parameter k represents the energy ratio of relativistic protons to electrons and is assumed to be 1 for our calculations, I_0 is surface brightness at measuring frequency which is 400 MHz in our case, and d is the source depth. The geometry of our sources is assumed to be cylindrical, and the cross-sectional diameter is taken as the source depth.

The estimated values of minimum particle energy (u_{min}), equipartition magnetic field strength B_{eq} of our remnant sources are given in Table 3. We note that the B_{eq} values for our remnants are found in the range of 1.8 μ G to 3.66 μ G, which are similar to that reported for the remnants studied in the literature, e.g., 1.0 μ G for BLOB1 (Brienza et al., 2016), 0.89–1.6 μ G for B2 0924+30 (Jamrozy et al., 2004; Shulevski et al., 2017), 2.7 μ G for NGC 1534 (Duchesne & Johnston-Hollitt, 2019) and 4.1 μ G for J1615+5452 (Randriamanakoto et al., 2020). The remnants in DDRGs also show the magnetic field strength of a few μ G (see Konar et al., 2012). To estimate the break frequencies ($\nu_{b, low}$ and $\nu_{b, high}$) and spectral ages of our remnants, we model their radio spectra by using the Broad-band Radio Astronomy ToolS (BRATS³; Harwood et al. (2013)) package. Given the remnant nature of our sources, we use CI_{OFF} model, also known as the KGJP model (Komisarov & Gubanov, 1994), which is a modified form of the continuous injection model (CI; Jaffe & Perola (1973)) with the inclusion of energy losses via synchrotron and inverse Compton emission, after the cessation of AGN activity. While fitting the radio spectra in the BRATS we provide input parameters B_{eq} and α_{inj} , and obtain output parameters such as the break frequencies (ν_{low} and ν_{high}), time-scales of active (t_{ON}) and remnant (t_{OFF}) phases, total source age (t_s), and the goodness of fit parameter reduced χ^2 . We point out that the accurate value of α_{inj} is not known a priori, and hence,

we begin with a value similar to $\alpha_{150\text{ MHz}}^{1.5\text{ GHz}}$ which is the low frequency spectral index available for our sample sources. The best fit values of α_{inj} for our sources are in the range -0.5 – -0.6 which are similar to the typical values measured in remnant and active radio galaxies (Murgia et al., 2011). Although, one of our sample sources GMRT022318-044526, the radio SED is best fitted with a somewhat lower value of $\alpha_{inj} = -0.4$ (see Table 3).

The modelled radio spectra of our sources are shown in Figure 2 (right panel), and the best-fit parameters are listed in Table 3. We note that our remnants show $\nu_{b, low}$ in the range of 250 MHz to 875 MHz above which their spectra steepen. The values of $\nu_{b, low}$ are consistent with the fact that our sources exhibit strong spectral curvature between 150 MHz and 1.5 GHz, i.e., $\alpha_{150\text{ MHz}}^{325\text{ MHz}} - \alpha_{400\text{ MHz}}^{1.5\text{ GHz}} \geq 0.5$. Although, in all sources, the $\nu_{b, high}$ above which spectrum falls off exponentially, lies outside the frequency coverage (>1.5 GHz) (see Table 3), and it is determined from the SED modelling. The knowledge of break frequencies allows us to obtain spectral age estimates. Based on the best spectral fits, we find the total spectral ages (t_s) of our remnants in the range of 20.3 Myrs to 41.4 Myrs. The duration of the active phase (t_{ON}) is in the range 14.5 Myr to 28.0 Myr, while sources have spent nearly 5.0 Myr to 26.0 Myr in the remnant phase (see Table 3). We note that the typical errors associated with the spectral ages (t_s , t_{ON} and t_{OFF}) are nearly 10 per cent. Although, the quoted errors are rendered by the model fittings and true uncertainties can be much larger owing to the several assumptions made in computing spectral ages (Harwood, 2017). Hence, we caution that the spectral age estimates should only be treated as characteristic timescales.

Further, we compute the average speed of lobes along the jet axis by dividing the average distance between centre and the outer edge of lobes with the timescale of active phase t_{ON} . We assume that our sources are lying in the plane of sky, i.e., the angle between the jet axis and the line-of-sight is 90°. For our remnants, we find that the average speeds of lobes are in the range of 0.01c to 0.07c, which are similar to those found for powerful radio galaxies (see O’Dea et al., 2009). In other words, dynamical ages, if derived using a typical average speed of lobes, would be

³<http://www.asknastronomer.co.uk/brats/>

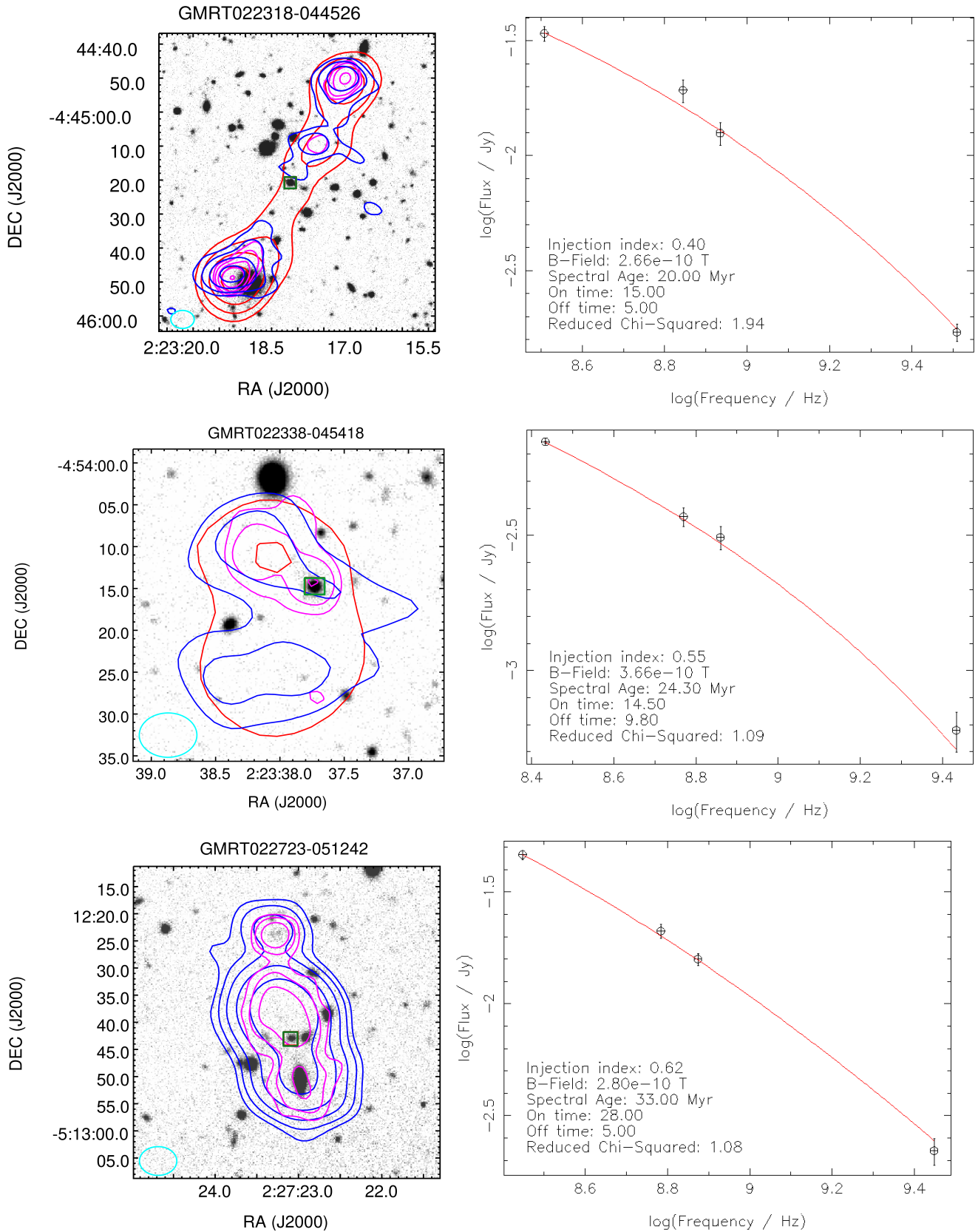


Figure 2: *Left panel:* The images of remnant sources. The radio contours of band-3 uGMRT (in Blue), 325 MHz (in Red), and 1.5 GHz JVLA (in Magenta) are overlotted on the corresponding HSC *i* band optical image. The radio contours are at $3\sigma \times (1, 2, 4, 8, 16, \dots)$ levels and the optical image is logarithmically scaled. The uGMRT band-3 synthesized beam of $6''.7 \times 5''.3$ is shown in the bottom left corner. The potential host galaxy of a remnant is marked with a green box around it. *Right panel:* The best fit radio SEDs of our remnant sources. The solid red curve represents model fitted to the data points.

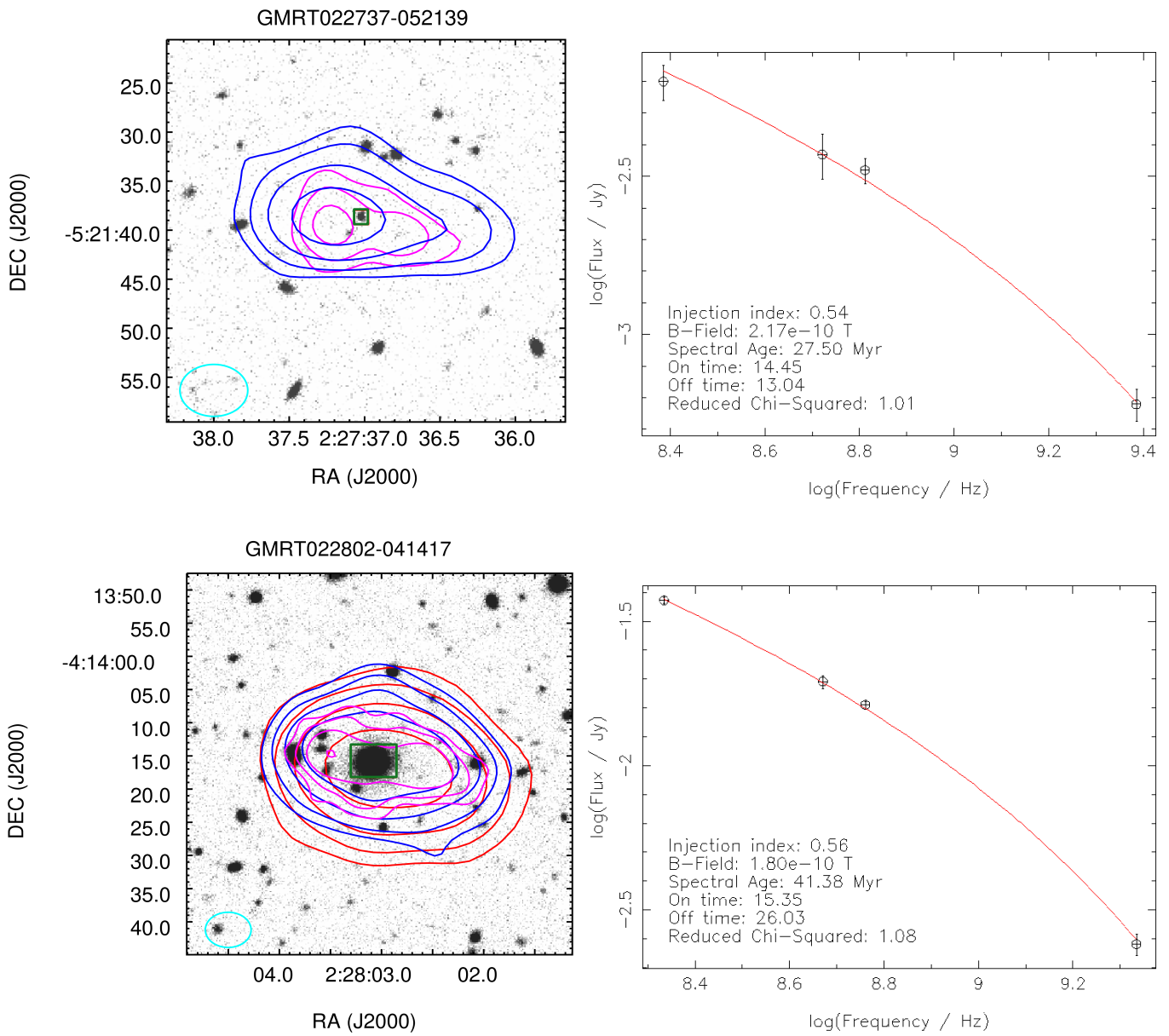


Figure 2: - continue

consistent with the spectral ages. We also examine the ratio of remnant age to total source age (t_{OFF}/t_s) which describes the fraction of total life a source spent in the remnant phase. For our remnant sources, we find t_{OFF}/t_s in the range of 0.16 to 0.63 (see Table 3). The wide range of t_{OFF}/t_s infers that our sources are in different phases of their evolution. One of the noteworthy examples in our sample is GMRT022802-041417, which has spent nearly 63 per cent of its total life in the remnant phase. The active phase duration of this source is only 15.4 Myr, while it has spent nearly 26.0 Myr in the remnant phase. Thus, we emphasize that despite the limited frequency coverage (150 MHz – 1.5 GHz) our observations are capable of detecting remnants in the different phases.

4.2 Comparison with other remnants

To understand the nature of our remnants, we compare their spectral ages with the previously studied remnant sources. The comparison sources include BLOB1 (Brienza *et al.*, 2016), B2 0924+30 (Shulevski *et al.*, 2017), J1615+5452 (Randriamanakoto *et al.*, 2020), NGC 1534 (Duchesne & Johnston-Hollitt, 2019), four sources from Murgia *et al.* (2011) and nine sources from Parma *et al.* (2007). In Figure 3, we show a plot of total source age (t_s) versus fractional remnant duration (t_{OFF}/t_s). It is evident that our sample remnants have systematically lower spectral ages than that for most of the remnant sources. There are only three sources, in addition to our five sample sources that have spectral ages <50 Myr. However, we note that a simple comparison of the spectral ages in a heterogeneous sample of remnants may not yield meaningful insights considering the fact that source age depends on various factors such as physical radio size, magnetic field, large-scale environment and redshift (Turner, 2018). Therefore, we consider the effects of these parameters in our further discussion.

We note that Murgia *et al.* (2011) found a longer duration of source ages ($t_s > 50$ Myr) for their remnant sources residing in cluster environments. The longer age for sources residing in clusters can be attributed to the slow or arrested expansion of lobes due to the high pressure of the dense intra-cluster medium. Hence, fading lobes of a remnant can last longer if energy losses due to dynamical effects are insignificant or absent (Murgia *et al.*, 2011). We point out that most of the remnant sources presented in Parma *et al.* (2007) also reside in cluster environments, and hence, they show high spectral ages. There are only three sources in the sample of Parma *et al.* (2007) with $t_s < 50$ Myr. Two of these sources with small values of t_{OFF}/t_s are recently switched-off sources and show unusually small radio sizes (<10 kpc). The relatively short source ages

can be understood as jets and lobes taking less time to grow to the smaller sizes. The radio sizes of our remnants, in the range of 190 kpc to 643 kpc, are similar to other remnants that show higher spectral ages. We point out that all our remnants with lower ages reside in non-cluster environments, while sources of similar radio sizes but higher spectral ages reside mostly in cluster environments. Hence, as expected, our sample sources residing in less dense environments fade away more rapidly due to the faster expansion of lobes. Thus, the relatively low spectral ages of our remnants, when compared to the remnants residing in cluster environments, can be partly attributed to the less dense large-scale environment.

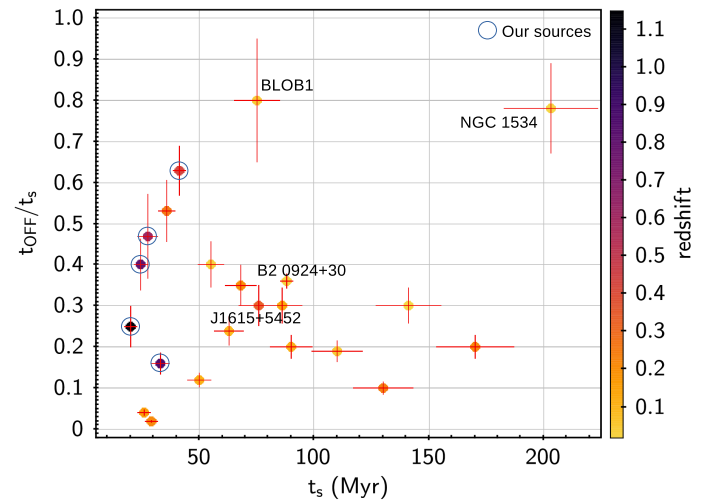


Figure 3: The plot of total source age t_s versus fractional remnant time-scale (t_{OFF}/t_s). The vertical colour bar indicates the redshifts of remnant hosts. The individually studied remnant sources are marked by their popular names. Our sample sources are marked by large Blue circles.

Further, remnants with large radio sizes are expected to show high spectral ages owing to the fact that jets and lobes take a longer time to traverse longer distances and to fill up large volumes. Both BLOB1 and NGC 1534 are the examples of old large-size remnants with their radio sizes spanning up to nearly 700 kpc and 600 kpc, respectively (see Brienza *et al.*, 2016; Duchesne & Johnston-Hollitt, 2019). The spectral ages of BLOB1 and NGC 1534 are 75 Myr and 203 Myr, respectively. The high value $t_{\text{OFF}}/t_s \sim 0.8$ confirms them to be old remnants that have spent nearly 80 per cent of their life in the remnant phase. Therefore, high spectral ages of BLOB1 and NGC 1534 remnants can be attributed to the combined effects of large radio size and long duration of the remnant phase. We note that one of our sample sources GMRT022318-044526 has

the radio size of 643 kpc, but it has source age (t_s) of only 20.3 Myr. The low value of $t_{\text{OFF}}/t_s = 0.25$ suggests it to be a relatively younger remnant. Notably, GMRT022318-044526 reside at a much higher redshift ($z = 1.15$ (see Table 2). We would like to emphasize that all our sample sources are at relatively higher redshifts ($z \sim 0.44\text{--}1.15$) which is evident from Figure 3. At high redshifts, inverse Compton losses dominate owing to the high density of Cosmic Microwave Background (CMB) photons. The inverse Compton equivalent magnetic field (B_{CMB}) scales with $(1+z)^2$ (see equation 1). Thus, due to increased inverse Compton losses, remnant sources at higher redshifts are expected to fade away much faster than their counterparts at lower redshifts. Hence, relatively lower spectral ages of our remnants can be largely attributed to their high redshifts.

We note that, to nullify the effects of the environment, radio size and redshift, one should compare remnants matched in these parameters. However, due to the paucity of remnant sources, we do not have such a comparison sample. It is worth mentioning that one remnant source WNB1127.5+4927 in the sample of Parma *et al.* (2007) is reported to reside in non-cluster environment at redshift $z = 0.25$ with its radio size of 211 kpc. The WNB1127.5+4927 shows similarity with our sample sources in terms of environment, size, and redshift, and hence, as expected, it has $t_s = 36$ Myr and $t_{\text{OFF}} = 19$ Myr, similar to our remnants. The remnant source J1615+5452 residing in non-cluster environments at $z = 0.33$ and radio size of 100 kpc, is also similar to our remnants, but it is reported to have higher spectral age with $t_s = 76$ Myr and $t_{\text{OFF}} = 22$ Myr (see Randriamanakoto *et al.*, 2020). A careful inspection of the spectral fitting of this source reveals that a statistically better fit with reduced $\chi^2 = 1.42$ yields $t_s = 35.9$ Myr and $t_{\text{OFF}} = 21.5$ Myr, although it requires unusually flat $\alpha_{\text{inj}} = 0.4$ and a high value of $B_{\text{eq}} = 12 \mu\text{G}$. We emphasize that a more robust spectral modelling using flux densities measured across a wide range of frequencies is required. In this context, the role of deep multi-frequency radio surveys is discussed in the next Section.

5. Potential of deep radio continuum surveys from the SKA and its pathfinders

Our full synthesis band-3 uGMRT observations have provided sensitive images with noise-rms down to $30 \mu\text{Jy beam}^{-1}$ and angular resolution of $6''.7 \times 5''.3$. Owing to its depth and angular resolution, we discovered wing-shaped radio morphology in one of our sample sources GMRT022338-045418. The diffuse

emission of low-surface-brightness related to the southern component of this source is completely missed in the 1.5 GHz JVLA observations. Previous less sensitive 325 MHz GMRT observations with somewhat coarser resolution ($10''.2 \times 7''.9$) could not decipher radio structures in GMRT022338-045418 (see Figure 2). Therefore, in the context of ongoing and planned deep radio continuum surveys, our band-3 uGMRT observations can be considered as a test-bed for discovering remnants possessing diffuse low-surface-brightness emission. For instance, the Evolutionary Map of the Universe (EMU) survey conducted with the Australian Square Kilometer Array Pathfinder (ASKAP) at 944 MHz provides deep continuum images with noise-rms of $25\text{--}30 \mu\text{Jy beam}^{-1}$ and resolution of $11''\text{--}18''$ over a large area of 270 deg^2 (Norris *et al.*, 2021). Despite being at a relatively higher frequency, EMU is capable of discovering large-scale diffuse emission owing to the short baselines up to 22m available in the ASKAP.

Recently, in a small area of 8.3 deg^2 of GAMA-23 field Quici *et al.* (2021) identified ten remnant candidates by using 119–216 MHz Murchison Wide-field Array (MWA) observations, 400 MHz uGMRT observations, 944 MHz EMU survey, and 5.5 GHz Australian Telescope of Compact Array (ATCA) observations. The multi-frequency observations were used to build broad-band SEDs and confirm the remnant status of radio galaxies. We emphasize that recent studies indicate remnant sources to be more abundant than that thought earlier. For instance, Singh *et al.* (2021) used the spectral curvature criterion and identified a large sample of 48 small-size ($<30''$) remnant candidates in 12.5 deg^2 area in the *XMM-LSS* field. The majority of small-size remnants are found at higher redshift ($z > 1.0$). In the *XMM-LSS* field, we also identified 21 large-size ($>30''$) remnant candidates which show distinct double-lobe morphology with absent core and tend to be more powerful ($L_{150 \text{ MHz}} > 10^{25} \text{ W Hz}^{-1}$) radio sources (Dutta *et al.* 2022, *under review*). Thus, remnant searches performed in the deep fields have demonstrated the existence of a variety of remnant sources residing across a wide range of redshifts. Although, most of the searches in the deep field are limited to only a small sky-area of a few deg^2 and rendered only small samples. The large-area deep surveys have the potential to discover a large population of remnants that would offer better insights into the evolution of radio galaxies in the remnant phase.

In Section 4., we pointed out that the radio observations over a wide range of frequencies are needed for robust determination of spectral ages of remnants. The upcoming radio continuum surveys from the SKA telescope covering a wide range of frequencies, *i.e.*, 50 MHz – 350 MHz with SKA1-low, and 350 MHz –

15.3 GHz with SKA1-mid would be ideal for spectral modelling. As per the baseline design performance, SKA1-mid is expected to provide noise-rms of $4.4 \mu\text{Jy beam}^{-1}$ in one hour observing time in the 0.35–1.05 GHz band centered at 770 MHz (see SKA factsheet⁴). Thus, the large-area multi-frequency deep radio surveys from the SKA and its pathfinder are expected to unveil a large population of remnants distributed over different evolutionary phases.

6. Conclusions

In this paper, we presented the new band-3 uGMRT observations of five remnant sources selected based on the strong spectral curvature, emission of low-surface-brightness from lobes, and absent radio core in the 3.0 GHz VLASS images. We performed modelling of radio SEDs using observations from the LOFAR at 144 MHz, GMRT at 325 MHz, uGMRT at 400 MHz (band-3) and JVLA at 1.5 GHz. The salient results of our study are outlined as below.

- With our deep full synthesis band-3 uGMRT observations (median noise-rms $\sim 30 \text{ mJy beam}^{-2}$) we confirm the presence of low-surface-brightness emission in all our five remnant sources. The surface brightness at 400 MHz is found in the range of $36 \text{ mJy arcmin}^{-2}$ to $201 \text{ mJy arcmin}^{-2}$, which is similar to those found in remnants studied in the literature (Brienza *et al.*, 2017).
- With our band-3 uGMRT observations, we discovered wing-shaped radio morphology in one of our sample sources GMRT022338-045418. Previous 325 MHz GMRT observations were unable to reveal structures due to its coarser resolution, while 1.5 GHz JVLA observations did not detect diffuse emission from the southern component. Both northern as well as southern components show two peaks that are similar to the primary and secondary lobes commonly seen in the Z-shaped and X-shaped radio sources. Despite its extended morphology, this source is faint with the total flux density of only $3.1 \pm 0.5 \text{ mJy}$ at 400 MHz, which in turn yields low surface-brightness of $36 \text{ mJy arcmin}^{-2}$.
- We fitted the radio SEDs with CI_{OFF} model that assumes a continuous injection phase for the duration of t_{ON} , and thereafter, a remnant phase for

the duration of t_{OFF} with total source age $t_s = t_{\text{ON}} + t_{\text{OFF}}$. For our remnant sources, the best fit models yield source ages (t_s) in the range of 20.3 Myr to 41.4 Myr.

- We find that our small sample of remnants shows a wide distribution of t_{OFF}/t_s in the range of 0.16 to 0.63. In other words, our sample sources have spent 16 per cent to 63 per cent of their total life in the remnant phase. Hence, our sources belong to the different phases of evolution.
- The estimated spectral ages of our remnants are, in general, lower than those found for several remnants previously studied in the literature. We caution that spectral age depends on various factors such as the radio size, magnetic field, redshift, and the large-scale environment, so we need to account for these parameters while comparing spectral ages. Notably, remnants residing in cluster environments show higher spectral ages due to less or insignificant dynamical energy losses from the reduced or absent expansion of lobes embedded within the dense intra-cluster medium. Further, we found that our remnant sources have systematically higher redshifts than most of the sources reported in the literature. Therefore, inverse Compton energy losses are more dominant for our high redshift sources, which in turn reduces their source ages.
- We note that the total source ages of our remnants are similar to one of the sample sources WNB1127.5+4927 of Parma *et al.* (2007), which has similar radio size, redshift, and environment.
- Our study, limited to a small sample lying within a small area of 2.3 deg^2 covered with one pointing of band-3 uGMRT observations, demonstrates the potential of deep large-area surveys from the SKA and its pathfinders. Based on our study, we expect a large population of remnants to be detected with the ongoing and planned deep radio continuum radio surveys.

Acknowledgements

We thank the anonymous reviewer for carefully reading the manuscript and giving valuable comments that improved the manuscript. SD, VS and AK acknowledge the support from the Physical Research Laboratory, Ahmedabad, funded by the Department of Space, Government of India. CHI and YW acknowledge the support of the Department of Atomic Energy, Government of India, under project no. 12-R&D-TFR5.02-

⁴<https://www.skatelescope.org/wpcontent/uploads/2018/08/16231-factsheet-telescopes-v71.pdf>

0700. We thank the staff of GMRT who have made these observations possible. GMRT is run by the National Centre for Radio Astrophysics of the Tata Institute of Fundamental Research. This paper is based on data collected from the Subaru Telescope and retrieved from the HSC data archive system, which is operated by the Subaru Telescope and Astronomy Data Center (ADC) at NAOJ. Data analysis was in part carried out with the cooperation of Center for Computational Astrophysics (CfCA), NAOJ.

References

- Bera, S., Sasmal, T. K., Patra, D., & Mondal, S. 2022, *ApJS*, 260, 7
- Brienza, M., Morganti, R., Shulevski, A., Godfrey, L., & Vilchez, N. 2016, *Astronomische Nachrichten*, 337, 31
- Brienza, M., Godfrey, L., Morganti, R., *et al.* 2017, *A&A*, 606, A98
- Cordey, R. A. 1987, *MNRAS*, 227, 695
- Duchesne, S. W., & Johnston-Hollitt, M. 2019, *PASA*, 36, e016
- Dwarakanath, K. S., & Kale, R. 2009, *ApJL*, 698, L163
- Godfrey, L. E. H., Morganti, R., & Brienza, M. 2017, *MNRAS*, 471, 891
- Govoni, F., & Feretti, L. 2004, *International Journal of Modern Physics D*, 13, 1549
- Gupta, Y., Ajithkumar, B., Kale, H. S., *et al.* 2017, *Current Science*, 113, 707
- Hale, C. L., Williams, W., Jarvis, M. J., *et al.* 2019, *A&A*, 622, A4
- Hardcastle, M. J., & Croston, J. H. 2020, *NewAR*, 88, 101539
- Harwood, J. J. 2017, *MNRAS*, 466, 2888
- Harwood, J. J., Hardcastle, M. J., Croston, J. H., & Goodger, J. L. 2013, *MNRAS*, 435, 3353
- Heywood, I., Hale, C. L., Jarvis, M. J., *et al.* 2020, *MNRAS*, 496, 3469
- Hota, A., Sirothia, S. K., Ohyama, Y., *et al.* 2011, *MNRAS*, 417, L36
- Jaffe, W. J., & Perola, G. C. 1973, *A&A*, 26, 423
- Jamrozy, M., Klein, U., Mack, K. H., Gregorini, L., & Parma, P. 2004, *A&A*, 427, 79
- Jarvis, M. J., Bonfield, D. G., Bruce, V. A., *et al.* 2013, *MNRAS*, 428, 1281
- Jurlin, N., Brienza, M., Morganti, R., *et al.* 2021, *A&A*, 653, A110
- Jurlin, N., Morganti, R., Brienza, M., *et al.* 2020, *A&A*, 638, A34
- Kardashev, N. S. 1962, *Soviet Ast.*, 6, 317
- Komissarov, S. S., & Gubanov, A. G. 1994, *A&A*, 285, 27
- Konar, C., Hardcastle, M. J., Jamrozy, M., Croston, J. H., & Nandi, S. 2012, *MNRAS*, 424, 1061
- Lacy, M., Baum, S. A., Chandler, C. J., *et al.* 2020, *PASP*, 132, 035001
- Lal, D. V. 2021, *ApJ*, 915, 126
- Lal, D. V., Sebastian, B., Cheung, C. C., & Pramesh Rao, A. 2019, *AJ*, 157, 195
- Mahatma, V. H., Hardcastle, M. J., Williams, W. L., *et al.* 2018, *MNRAS*, 475, 4557
- . 2019, *A&A*, 622, A13
- Mohan, N., & Rafferty, D. 2015, *PyBDSF: Python Blob Detection and Source Finder*, ascl:1502.007
- Morganti, R. 2017, *Nature Astronomy*, 1, 596
- Murgia, M., Parma, P., Mack, K. H., *et al.* 2011, *A&A*, 526, A148
- Nandi, S., & Saikia, D. J. 2012, *Bulletin of the Astronomical Society of India*, 40, 121
- Norris, R. P., Marvil, J., Collier, J. D., *et al.* 2021, *PASA*, 38, e046
- O’Dea, C. P., Daly, R. A., Kharb, P., Freeman, K. A., & Baum, S. A. 2009, *A&A*, 494, 471
- Parma, P., Murgia, M., de Ruiter, H. R., *et al.* 2007, *A&A*, 470, 875
- Perley, R. A., Chandler, C. J., Butler, B. J., & Wrobel, J. M. 2011, *ApJL*, 739, L1
- Quici, B., Hurley-Walker, N., Seymour, N., *et al.* 2021, *PASA*, 38, e008
- Randriamanakoto, Z., Ishwara-Chandra, C. H., & Taylor, A. R. 2020, *MNRAS*, 496, 3381
- Saikia, D. J. 2022, *arXiv e-prints*, arXiv:2206.05803

- Saikia, D. J., & Jamrozy, M. 2009, Bulletin of the Astronomical Society of India, 37, 63
- Saripalli, L. 2012, AJ, 144, 85
- Shabala, S. S., Jurlin, N., Morganti, R., *et al.* 2020, MNRAS, 496, 1706
- Shulevski, A., Morganti, R., Harwood, J. J., *et al.* 2017, A&A, 600, A65
- Singh, V., Dutta, S., Wadadekar, Y., & Ishwara-Chandra, C. H. 2021, Galaxies, 9, 121
- Singh, V., Beelen, A., Wadadekar, Y., *et al.* 2014, A&A, 569, A52
- Slee, O. B., Roy, A. L., Murgia, M., Andernach, H., & Ehle, M. 2001, AJ, 122, 1172
- Swarup, G. 1991, in Astronomical Society of the Pacific Conference Series, Vol. 19, IAU Colloq. 131: Radio Interferometry. Theory, Techniques, and Applications, ed. T. J. Cornwell & R. A. Perley, 376–380
- Tamhane, P., Wadadekar, Y., Basu, A., *et al.* 2015, MNRAS, 453, 2438
- Tasse, C., Röttgering, H. J. A., Best, P. N., *et al.* 2007, A&A, 471, 1105
- Tasse, C., Cohen, A. S., Röttgering, H. J. A., *et al.* 2006, A&A, 456, 791
- Turner, R. J. 2018, MNRAS, 476, 2522
- van Haarlem, M. P., Wise, M. W., Gunst, A. W., *et al.* 2013, A&A, 556, A2